Geophysical Journal International

*Geophys. J. Int.* (2014) **196,** 243–252
Advance Access publication 2013 October 17

doi: 10.1093/gji/ggt391

# Origin of water layer multiple phases with anomalously high amplitude in near-seafloor wide-angle seismic recordings

Adrià Meléndez,[1] Valentí Sallarès,[1] César R. Ranero[2] and Jean Kormann[1,*]

[1]*Barcelona Center for Subsurface Imaging, Institut de Ciències del Mar (CSIC), Barcelona, Spain. E-mail: melendez@icm.csic.es*
[2]*Barcelona Center for Subsurface Imaging, ICREA at Institut de Ciències del Mar (CSIC), Barcelona, Spain*

Accepted 2013 September 23. Received 2013 September 20; in original form 2013 August 15

## SUMMARY

Water layer multiple seismic phases are recorded at ocean bottom seismometers and hydrophones as arrivals that correspond to the reflection of the primary phases at the sea–free air interface. In regions of low to moderate seabed relief, the shape of these phases mimics that of the primary phases with a traveltime delay that depends on the water layer thickness at the receiver location. Given their longer travel paths, multiple phases should have smaller amplitudes than their corresponding primary phases. However, depending on the geological context it can be relatively common to observe the opposite, which results in the identification of the multiple phases at longer offsets than the primary events. In this paper, we examine the origin of this apparently paradoxical phenomenon by analysing the combined effect of the major factors potentially involved: the source frequency content, the subsurface velocity distribution, the receiver–seafloor distance, the geometrical spreading and attenuation of sound waves and the ambient noise level. We use synthetic modelling to show that for certain combinations of these factors, the interference between the multiple and its reflection at the seafloor is constructive and has a higher amplitude than the primary wave. Our analysis indicates that in the most favourable cases the phases resulting from this interference can be observed at offsets some tens of kilometres longer than their corresponding primary phases, and thus they can provide useful information for velocity modelling.

**Key words:** Numerical approximations and analysis; Controlled source seismology; Site effects; Wave propagation.



## 1 INTRODUCTION

The goal of traveltime modelling of refraction and wide-angle reflection seismic (WAS) data is producing models of the earth's interior that describe the wave propagation velocity and the reflectors' geometry based on the recorded seismic phases. Typical *P*-wave propagation velocities vary from $\sim$1.6 km s$^{-1}$ for shallow sediments to $\sim$8 km s$^{-1}$ for the uppermost mantle rocks. As a consequence of this vertical velocity gradient, the refracted waves are only recorded for source–receiver offsets above a critical threshold (Červený 2001). Thus, the minimum offset necessary for an experiment mainly depends on the vertical velocity gradient and target depth. For conventional crust and uppermost mantle WAS studies, the minimum offset to record upper-mantle refractions is $\sim$30 km for 6-km-thick oceanic crust, while it can be >150 km for 40-km-thick continental crust. As a rule of thumb, the ratio between the resolved depth and the recording offset in WAS experiments is approximately 1:4, so observing refracted phases at the longest possible offsets is key to retrieving information on the deepest levels of interest.

In marine experiments, seismic waves are usually generated by air gun shots, and recorded by ocean bottom seismometers and/or hydrophones (OBS/H). The data are typically represented as record sections for each OBS/H, in which the seismic traces are plotted against the source–receiver offset (Fig. 1). In these records, reflections appear as deformed hyperbolas and refractions as curves whose local slope is proportional to their average propagation velocity at a given depth. The maximum distance at which the seismic signal is detected results from a combination of different factors, including the source energy, the amplitude decay by geometrical spreading and attenuation, the transfer function and seafloor coupling of the receiver and the ambient noise level.

The water layer multiple in marine seismic records results from the reflection of primary phases (both refractions and reflections) at the sea–free air interface. Given that the water layer has an approximately constant velocity, the multiple imitates the shape of the primary phases with a traveltime delay that depends on the

*Now at: Barcelona Supercomputing Center, Barcelona, Spain.

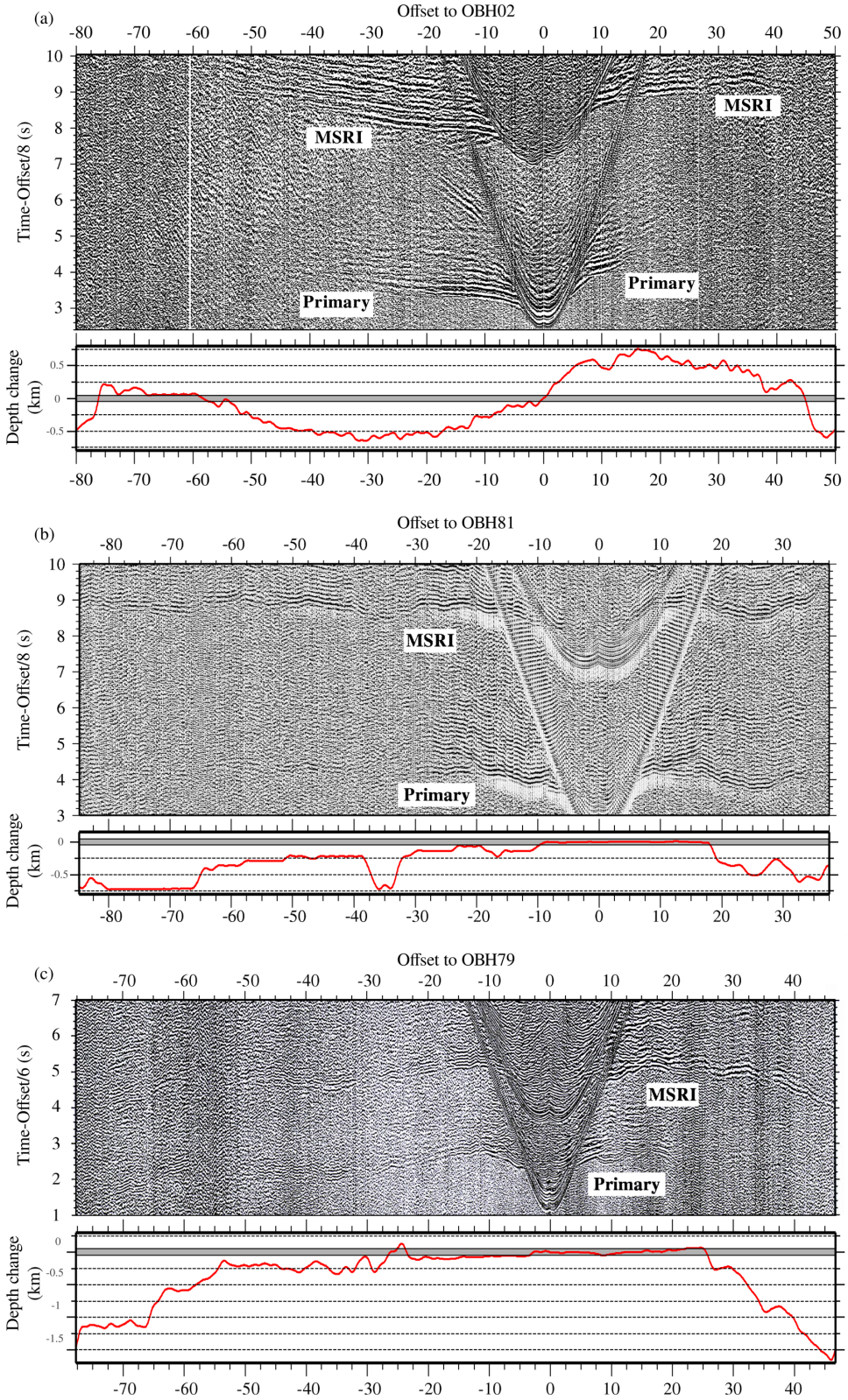


**Figure 1.** Three examples of record sections in which the MSRI (multiple–seafloor reflection interference) phase can be followed to longer offsets than its corresponding primary phase: (a) OBH02 from the Mid-Atlantic Expedition 2003/2004 (M60/2) aboard R/V Meteor (Dannowski *et al.* 2011), (b) OBH81 from the MEDOC-2010 survey (Prada *et al.* 2012) and (c) OBH79 from the Paganini-1999 survey (Sallarès *et al.* 2003). Primary and MSRI phases are labelled. The panels below each record section show the change in bathymetry along the profile relative to the depth at the receiver location. The grey band marks the ±50 m range of depth difference for which the source–receiver multiple interference can occur.

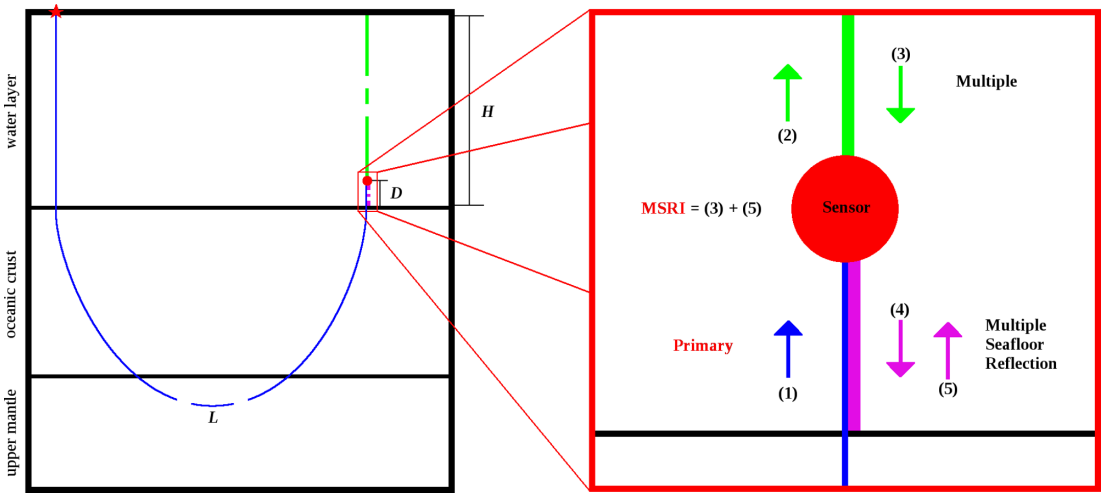


**Figure 2.** General modelling scheme for our synthetic test. The ray path is divided into three significant segments using different colours. Normal thickness and double thickness indicate one- and two-way ray path segments, respectively. (Right red box) Modelling scheme for the first part of the test in which we calculate $r_0$ values. Arrows indicate the directions of the ray path segments associated with the different waves, and are numbered in chronological order. The phases named in red, primary and MSRI, are those that can actually be observed on record sections. (Left black box) Modelling scheme for the second part of the test in which we calculate $\Delta L$ values. Source and sensor locations are marked with a star and a circle, respectively. $L$ is the ray path length from source to receiver, $H$ is the water layer thickness at the receiver location, and $D$ is the receiver–seafloor distance. The blue segment has length $L$ and corresponds to the primary phase ray path. The green segment has length $2(H - D)$ and together with the blue one they form the multiple phase ray path ($L + 2H - 2D$). The purple segment has length $2D$ and with the other two segments they correspond to the ray path for the seafloor reflection of the multiple ($L + 2H$). All three segments include a dashed portion to signify that $L$, $H$ and $D$ are variable parameters in our synthetic test. Note that we keep a constant water depth at the source location ($L_w$), so that in general it does not coincide with variable $H$.

water depth. Backus (1959) formulated the detrimental effect of water layer reverberations on near-vertical reflection seismic data as a linear filtering mechanism, and explored inverse filtering techniques to reduce it. His formulation for the signal recorded at the receiver can be shown to be consistent with our own. However, unlike in near-vertical seismic data, in WAS experiments water layer multiples hardly ever deteriorate the data quality and are commonly disregarded because they simply duplicate the information provided by the primary phases. Furthermore, being a secondary reflection, its amplitude should be consistently smaller than that of the corresponding primary wave. However, some recordings show multiple phases that can be followed to longer offsets than primary ones (Fig. 1), meaning that the amplitude of the primary phase is below the noise level, while the amplitude of the multiple is above it. In certain cases, the multiple is visible tens of kilometres farther than the primary waves, thus providing information on the velocity structure at deeper crustal levels that could not be retrieved from the primary phases. In terms of modelling, using these data would result in denser ray coverage and longer ray paths. In this regard, there are a few examples of the usage of multiple phases in traveltime modelling (e.g. Muller *et al.* 1999; Minshull *et al.* 2006), although they are usually discarded. Often used but typically not discussed procedures are either to convert multiple picks to the traveltime expected for their corresponding primary phases or to visually inspect multiple phases to roughly guide the extrapolation of weak primary phase picks. Nonetheless, water layer multiples have been successfully used in other applications, such as the improvement of OBS data quality with supervirtual refraction interferometry (Bharadwaj *et al.* 2013), the broadening of the subsurface illumination obtained by mirror imaging (Dash *et al.* 2009) or the determination of a 2-D velocity model of the water layer by ray tracing forward modelling (Grad *et al.* 2011).

In this work, we study this phenomenon, present a hypothesis to explain it and test it with a synthetic modelling scheme that evaluates the weight of potential key factors involved. In the first part of the test, we generate synthetic seismograms with a 1-D finite-difference wave equation solver (Kormann *et al.* 2011), whereas in the second part, we approximate the effects of geometrical spreading, wave attenuation and ambient noise. We obtain a rough measure of the possible offset gain, and infer the most propitious geological conditions for this phenomenon to take place.

## 2 HYPOTHESIS: CONSTRUCTIVE INTERFERENCE

Some seismic records show a multiple-like phase that can be followed to longer offsets than the corresponding primary phases, meaning that it remains above the noise level when primary phases are below it (Fig. 1). Also, even when both phases are observed up to similar offsets, it sometimes happens that the multiple phase is more clearly defined and thus easier to follow. Thus, the multiple amplitude must somehow be increased, compensating for the amplitude loss associated to longer wave propagation. Our working hypothesis is that, for sensors located close to the seafloor, the receiver multiple and its reflection at the seafloor interfere constructively, generating a signal with amplitude higher than that of the primary phases (right red box in Fig. 2). This constructive interference is possible because the reflection of the multiple at seafloor does not involve a phase inversion. For simplicity, from here on we term it the 'multiple–seafloor reflection interference' (MSRI) to refer to the observation on seismic data, that is the seismic phase on record sections, and limit 'multiple' to indicate the reflection of primary waves at the sea–free air interface.

An alternative to our working hypothesis is that the phenomenon is caused by the constructive interference between the source multiple (reflection at the seafloor and at the water surface before entering the subsurface) and the reflection at the seafloor of the receiver

multiple. However, it must be noted that this interference might only occur if the water depths at the source ($H_{SM}$) and receiver ($H_{RM}$) locations happen to be sufficiently similar. Indeed, for one-cycle sine waves with 10 Hz frequency, typical of WAS records, such interference would only produce an amplitude greater than the primary wave for $|H_{SM} - H_{RM}| < 50$ m. Thus, the source multiple will only consistently contribute to the continuity of the multiple-like phase in the record section if the bathymetry along the profile segment corresponding to the shots that produce such phase is almost horizontal. Such a sustained coincidence in source and receiver water depth is hardly ever encountered in any of the tens of record sections from different experiments showing the anomalously high multiple amplitude that we have inspected in the course of this work. Still, it is worth mentioning that there are certain geological contexts in which this may occur, such as oceanic abyssal plains. Fig. 1 displays the variation in bathymetry along the profiles with respect to the depth at the receiver location to show that the multiple-like phase with higher amplitude than the primary is almost always observed at offsets for which the depth difference is much greater than 50 m. In summary, it is clear that the MSRI, which is independent of changes in seafloor depth, is far more general than the source–receiver multiple interference. This is the reason why we have centred our numerical analysis on the MSRI.

We identified three key factors that potentially control the MSRI. Two of them are related to acquisition: the source frequency and the seafloor–receiver distance. The third one is the velocity field in the shallow subsurface material defining the acoustic impedance. Also, we need to account for two potential causes of amplitude loss: geometrical spreading and wave attenuation. The amplitude decay associated to the reflection at the sea–free air interface is of ∼0.05 per cent ($R_{w-a} \approx -0.9995$), so that we do not need to consider it in our modelling scheme, that is, we assume $R_{w-a} = -1$ (Backus 1959). While this approximation is generally considered to be valid for typical marine seismic experiments, it does not hold for higher frequencies, and particularly under rough sea conditions (Liu & Huang 2001).

One last factor to be considered is ambient noise, which limits the observable offset for primary and MSRI phases on record sections. The additional offset obtained from the MSRI phase implies an increase in the length of the ray paths used in modelling. Therefore, source-to-receiver ray path length is a good parameter to quantitatively measure the improvement obtained by including MSRI picks in WAS data modelling.

## 3 SYNTHETIC MODELLING

### 3.1 Measuring the interference

We first evaluated the ratio ($r_0$) between the peak amplitude of the MSRI and the reference peak amplitude of an incident multiple wave to determine the conditions that produce a constructive interference ($r_0 > 1$). The $r_0$ parameter can be understood as the value that scales the peak amplitude of the multiple phase to give the MSRI peak amplitude. The factors inferred to control the interference (source frequency band, receiver–seafloor distance and subsurface velocity) are parametrized in our synthetic modelling scheme, and each parameter is assigned a realistic study range, defining the set of parameter combinations to be tested.

For multiple waves the propagation near the receiver is quasi-vertical and the plane wave approximation can be assumed, so that the interference can be studied in one dimension. We used shot1D, a 1-D acoustic wave propagation code developed by Kormann *et al.* (2011) to generate the synthetic data needed to calculate $r_0$ (Fig. 3). Synthetic traces are obtained by defining the source (a Ricker wavelet) and receiver locations. The medium is defined by the velocity values assigned to an array of depth nodes, and is assumed to be incompressible. Density effects in the water column are considered to be of second order and neglected. The propagation is modelled with a time-domain finite-difference scheme of sixth order in space and second order in time defined by

$$\frac{1}{c^2(z)} \cdot \frac{\partial^2 p(z,t)}{\partial t^2} = \nabla^2 p(z,t), \quad (1)$$

where $p$ is pressure, $z$ is depth, $t$ is time and $c$ is sound speed. Time increment is set to fulfil the Courant–Friedrichs–Lewy condition (Courant *et al.* 1967). The upper end of the model is defined as a free-surface condition by setting $u(0, t) = 0$, which implies total reflection at the top of the medium. The lower end of the model is an absorbing boundary made of complex frequency-shifted perfectly matched layers (Kormann *et al.* 2009). This simulates a half-space propagation, avoiding undesired reflection artefacts from the bottom.

Within shot1D, the source frequency band is parametrized by setting the central frequency of the wavelet ($F$), while the receiver–seafloor distance ($D$) is set by the location of the receiver with respect to the seafloor defined in our velocity model. The dominant frequency in long-offset WAS marine experiments is typically centred around 10 Hz, with the main energy spectrum between ∼5 and 15 Hz, but we considered a wider range of 4–30 Hz, with 0.5 Hz sampling rate, to cover a greater variety of experimental cases. The receiver–seafloor distance ($D$) may vary from one instrument to another, and we tested the range 0–10 m, at 1-m interval (see Table 1).

We parametrized the subsurface velocity distribution in depth ($z$) as a constant velocity gradient ($V(z) = V_0 + G \cdot z$) described by parameters $V_0$, the velocity immediately below the seafloor, and $G$, the velocity gradient. Above the subsurface, water velocity was fixed to 1.5 km s$^{-1}$. The models were extended downward to a total depth of 10 km and the maximum velocity was limited to 6.5 km s$^{-1}$. We used a spatial increment of 0.1 m (d$x$), fine enough to sample the shortest wavelength considered. For $V_0$, we selected values between 1.6 km s$^{-1}$ (i.e. water-saturated sediments) and 4 km s$^{-1}$ (i.e. basement outcrops) with a sampling rate of 0.1 km s$^{-1}$, and for $G$, 0.5–2.5 s$^{-1}$, and a sampling rate of 0.5 s$^{-1}$, a wide range that encloses most experimental samples (e.g. White *et al.* 1984, 1992). See Table 1 for a compilation of the parameter values considered in this first part of the synthetic modelling.

The reference peak amplitude of the multiple wave was computed within the water layer avoiding any influence of the subsurface velocity field and the sea–free air interface. To do so, we located the source halfway through the water column and recorded its signal 1 m below it. The MSRI peak amplitude was measured at a distance $D$ above the seafloor simulating real OBS/H positions in experiments (Fig. 3). Note that $r_0$ depends on $F$ through both multiple and MSRI peak amplitudes, but on $D$, $V_0$ and $G$ only through the latter. Thus, $r_0$ includes the effects of $D$, $V_0$ and $G$ on the amplification of the multiple amplitude for each frequency $F$. Selected results for this first part of the test are shown in Fig. 4.

### 3.2 Amplitude decay

For the proper study of this phenomenon, we needed to compare the peak amplitudes of the primary and MSRI phases. To do so, we derived expressions for the peak amplitudes of these phases, using

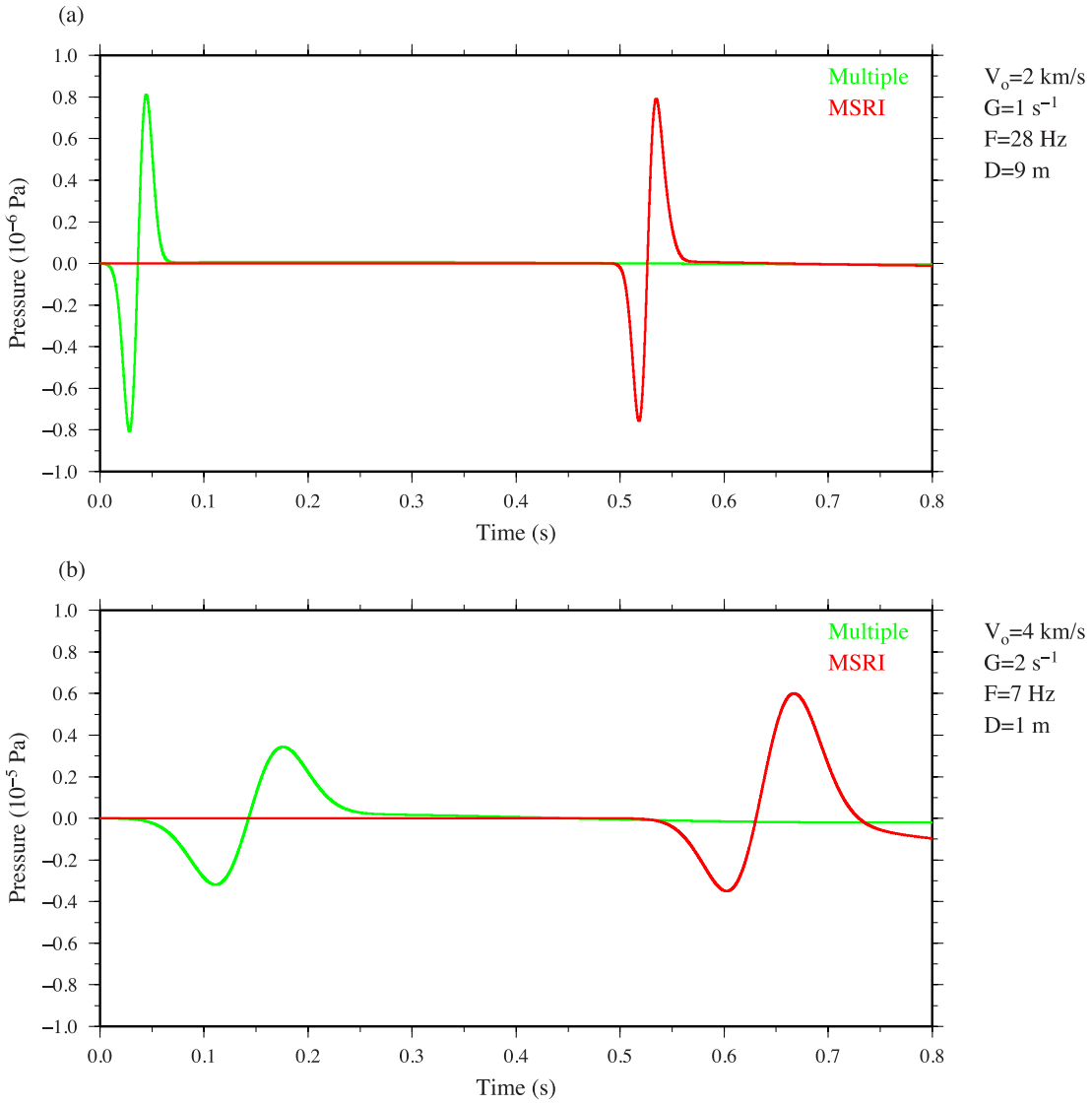


**Figure 3.** Selected examples of 1-D acoustic wave propagations performed with shot1D for (a) $r_0 \approx 0.98$ with $V_0 = 2\,\mathrm{km\,s^{-1}}$, $G = 1\,\mathrm{s^{-1}}$, $F = 28$ Hz, $D = 9$ m and (b) $r_0 \approx 1.75$ with $V_0 = 4\,\mathrm{km\,s^{-1}}$, $G = 2\,\mathrm{s^{-1}}$, $F = 7$ Hz, $D = 1$ m (black circles in Figs 4a and f, respectively). Green lines represent the traces recorded 1 m below the source from which we obtain the peak amplitudes of the incident multiple waves, whereas red lines represent the traces recorded at a distance $D$ above the seafloor, which provide the MSRI peak amplitudes.

**Table 1.** Ranges and sampling rates for the parameters involved in the calculation of $r_0$ with shot1D in the first part of the test.

| | $F$ (Hz) | $D$ (m) | $V_0$ (km s$^{-1}$) | $G$ (s$^{-1}$) |
|---|---|---|---|---|
| Range | 4–30 | 0–10 | 1.6–4 | 0.5–2.5 |
| Sampling (unit/sample) | 0.5 | 1 | 0.1 | 0.5 |

$r_0$ and accounting for the total amplitude loss. These expressions can be compared to the ambient noise level, which allowed us to compute the ray path length gained with the inclusion of the MSRI phase. The gain in ray path length implies an increase in maximum recording offset, and thus provides a quantitative measure of the benefit in using these data. The ray path length increment depends on $r_0$, the water layer thickness, the attenuation coefficients and the signal-to-noise ratio (SNR) at the receiver location.

The amplitude decay by geometrical spreading in a uniform medium is inversely proportional to the distance from the source, that is, the ray path length $L$ (Stein & Wysession 2003). The two waves interfering to create the MSRI phase have slightly different ray path lengths (left black box in Fig. 2): $L + 2H - 2D$ for the multiple, and $L + 2H$ for its reflection at the seafloor, where $L$ is the source-to-receiver ray path length, that is, the primary phase ray path length, and $H$ is the water layer thickness at the location of the OBS/H receiver. However, if $H \gg D$ we can approximate their ray path lengths to being equal:

$$L + 2H - 2D \approx L + 2H, \tag{2}$$

which implies that both interfering waves undergo basically the same amplitude loss by geometrical spreading, and that it can be ascribed to the MSRI. To derive a relation between the peak amplitudes of the primary and MSRI arrivals using $r_0$, it needs to be corrected to account for the effect of geometrical spreading as follows:

$$r(L, H, r_0) = r_0 \frac{\frac{1}{L+2H}}{\frac{1}{L}} = r_0 \frac{L}{L+2H}, \tag{3}$$

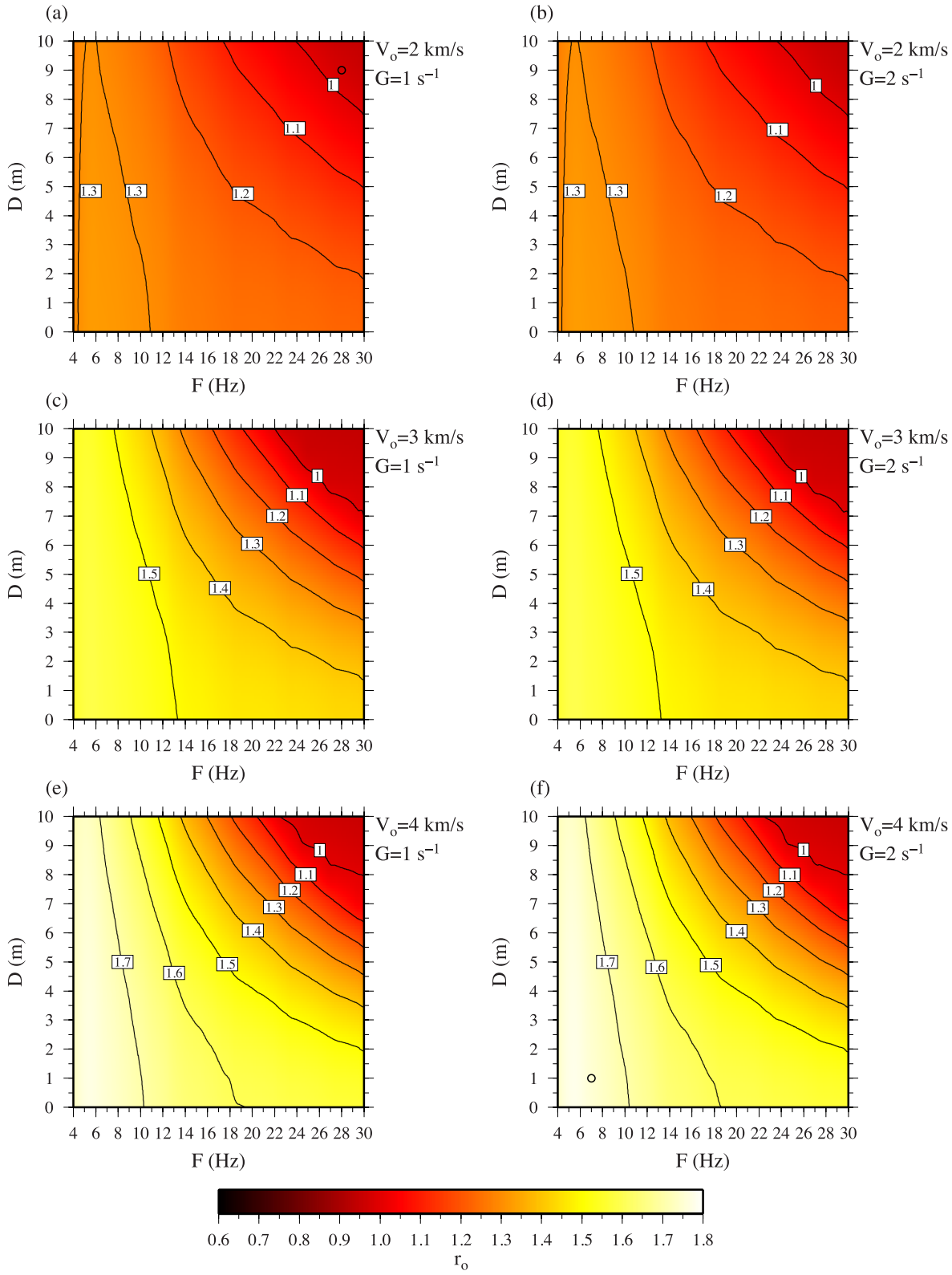


**Figure 4.** Diagrams of $r_0$ as a function of $F$ and $D$, each for a particular velocity model defined by $V_0$ and $G$: (a) $V_0 = 2\,\mathrm{km\,s^{-1}}$, $G = 1\,\mathrm{s^{-1}}$, (b) $V_0 = 2\,\mathrm{km\,s^{-1}}$, $G = 2\,\mathrm{s^{-1}}$, (c) $V_0 = 3\,\mathrm{km\,s^{-1}}$, $G = 1\,\mathrm{s^{-1}}$, (d) $V_0 = 3\,\mathrm{km\,s^{-1}}$, $G = 2\,\mathrm{s^{-1}}$, (e) $V_0 = 4\,\mathrm{km\,s^{-1}}$, $G = 1\,\mathrm{s^{-1}}$ and (f) $V_0 = 4\,\mathrm{km\,s^{-1}}$, $G = 2\,\mathrm{s^{-1}}$. Black circles mark the examples shown in Fig. 3.

where $1/L$ and $1/(L + 2H)$ are the correction factors for the geometrical spreading of the primary and MSRI arrivals, respectively, considering the source amplitude is measured at the unit distance.

Assuming a source of unit amplitude, the amplitude decay by geometrical spreading of the primary and MSRI phases can be written as:

$$A_p(L) = \frac{1}{L}, \tag{4}$$

$$A_M(L, H, r_0) = A_p r = \frac{1}{L} r_0 \frac{L}{L + 2H} = \frac{r_0}{L + 2H}. \tag{5}$$

The mathematical expression for the wave attenuation in the plane wave approximation for a source of unit amplitude is (Stein & Wysession 2003):

$$A(L) = \mathrm{e}^{-\sum_i a_i \cdot L_i}, \tag{6}$$

where $a_\mathrm{i}$ is the attenuation coefficient in inverse distance units, and $L_\mathrm{i}$ the segment of ray path affected by this particular coefficient. The attenuation coefficient is a function of the wave frequency ($F$), the propagation velocity ($V_\mathrm{i}$) and of the $Q_\mathrm{i}$ factor of the medium (Johnston & Toksoz 1981):

$$a_i = \frac{\pi F}{V_i Q_i}. \tag{7}$$

In order to model wave attenuation, we assumed that the ray first travels through a water layer of $L_\mathrm{w} = 4$ km, an approximate average of the oceanic water depth, and then through oceanic crust and upper mantle (left black box in Fig. 2). In addition, the MSRI ray travels through a water layer at the receiver location with variable thickness $H$. The attenuation in the water layer ($a_\mathrm{w}$) for the typical frequencies of WAS experiments is $\sim 10^{-8}$ m$^{-1}$ (Urick 1983). The $Q$ factor of oceanic crust and upper mantle is commonly found in a range from 10 to 1000 (e.g. Wilcock *et al.* 1992, 1995; White & Clowes 1994; Goldberg & Sun 1997; Swift *et al.* 1998). For the calculation of the attenuation coefficient, we also needed to select $F$ and $V$. For the former we picked 10 Hz, being the central frequency of the source spectrum in WAS data, and for the latter 6 km s$^{-1}$, a rough average of the medium velocity. With all these considerations, the three attenuation coefficients ($a_\mathrm{c}$) that we tried are $\sim 5 \times 10^{-4}$ ($Q = 10$), $\sim 5 \times 10^{-5}$ ($Q = 100$) and $\sim 5 \times 10^{-6}$ m$^{-1}$ ($Q = 1000$).

Using (6), expressions (4) and (5) are modified to account for attenuation as follows:

$$A_p(L) = \frac{1}{L} \mathrm{e}^{-a_w \cdot L_w} \mathrm{e}^{-a_c \cdot (L - L_w)}, \tag{8}$$

$$A_M(L, H, r_0) = \frac{r_0}{L + 2H} \mathrm{e}^{-a_w \cdot (L_w + 2H)} \mathrm{e}^{-a_c \cdot (L - L_w)}, \tag{9}$$

again considering the approximation in (2), meaning that we can also ascribe the amplitude loss by attenuation to the MSRI phase. Even though $a_\mathrm{w}$ is $\sim$2.5 orders of magnitude smaller than the smallest $a_\mathrm{c}$, we chose to include it in (8) and (9) because it depends on one of the parameters evaluated in this test, $H$.

For the evaluation of expressions (8) and (9), it is necessary to define realistic ranges for the three parameters involved ($L$, $H$ and $r_0$). Typical WAS profiles extend for $\sim$100–300 km, so that a rough approximation of the maximum source-to-receiver ray path length $L$ is $\sim$400 km. For a minimum $L$ value, we selected $L_\mathrm{min} = 10$ km, which yields 6 km of ray path through the crust ensuring that the test scanned all potentially significant $L$ values. Regarding $H$, most OBS/H are limited by construction to a maximum depth of $\sim$6 km, so we used 7 km as upper bound for this variable. For the lower bound, we imposed the condition that the longest wavelength be smaller than $H$ so we selected a minimum value of 500 m. The sampling rates were 10 m for $L$, and 1 m for $H$. The minimum $H$ value ensures the fulfilment of (2). The range of $r_0$ values was determined by the selection of 10 Hz as the frequency to obtain $a_\mathrm{c}$. As shown in Section 4, the maximum $r_0$ value for $F = 10$ Hz is $>$1.7, found for $D = 0$ m (Figs 4e and f). The bottom limit for $r_0$ is 1, and the sampling rate 0.01. This information is compiled in Table 2.

**Table 2.** Ranges and sampling rates for the parameters in expressions (8) and (9) used in the second part of the test. For the evaluation of these expressions, we also defined $a_\mathrm{c}$ ($5 \times 10^{-4}$–$5 \times 10^{-6}$) and $A_\mathrm{n}$ ($10^{-3}$–$10^{-9}$) ranges and sampled them by decades. $a_\mathrm{w}$ was set to a constant value of $1.15 \times 10^{-8}$.

| | $r_0$ | $L$ (km) | $H$ (km) |
|---|---|---|---|
| Range | 1–1.70 | 10–400 | 0.5–7 |
| Sampling (unit/sample) | 0.01 | 10 | 1 |

### 3.3 Ambient noise level

The ambient noise level determines the additional ray path length ($\Delta L$) gained from the MSRI data. For the calculation of $\Delta L$, we needed to compare expressions (8) and (9) with the noise level normalized to the source amplitude ($A_\mathrm{n}$), which is related to the SNR. For a source of unit amplitude, the SNR in dB and in amplitude units are defined as follows:

$$\mathrm{SNR(dB)} = 10 \log \left[\frac{1}{A_n}\right]^2 = 20 \log \left[\frac{1}{A_n}\right] = A_0\,(\mathrm{dB}) - A_n\,(\mathrm{dB}), \tag{10}$$

$$\mathrm{SNR} = \left[\frac{1}{A_n}\right]^2. \tag{11}$$

Combining (10) and (11) yields $A_\mathrm{n}$ as a function of the amplitudes in dB:

$$A_n = 10^{[[A_n(\mathrm{dB}) - A_0(\mathrm{dB})]/20]}. \tag{12}$$

We defined $\Delta L = L_\mathrm{M} - L_\mathrm{p}$, where $L_\mathrm{p}$ and $L_\mathrm{M}$ are the ray path lengths for which $A_\mathrm{p}$ and $A_\mathrm{M}$ intersect $A_\mathrm{n}$, respectively. Thus, $\Delta L > 0$ means that the MSRI phase is visible at greater ray path lengths than the primary phase, that is, the phenomenon is taking place. For simplicity, all $\Delta L < 0$ were set to 0, accounting for the cases in which the phenomenon does not occur. It is worth mentioning that while $\Delta L$ values illustrate the general behaviour, they should be taken as estimates because our amplitude decay correction is an approximation, and because noise will be range dependent if it is dominated by the previous shots.

Typical source amplitudes in WAS experiments are around 200 dB re 1 μPa at 1 m (e.g. Goold & Fish 1998; Cummings 2004; MacGillivray & Chapman 2005; Landrø & Amundsen 2010), and for the dominant frequencies, the noise level is found between $\sim$60 and $\sim$110 dB (Coates 2002). We picked approximate end-members for both the noise level (60 and 120 dB) and the source amplitude (180 dB re 1 μPa at 1 m and 240 dB re 1 μPa at 1 m). The end-members define a range of $A_\mathrm{n}$ between $10^{-3}$ and $10^{-9}$ that we sampled by decades. See Table 2 for a compilation of the parameter values used in this second part of the synthetic modelling. A selection of the results is displayed in Fig. 5 and in Table 3.

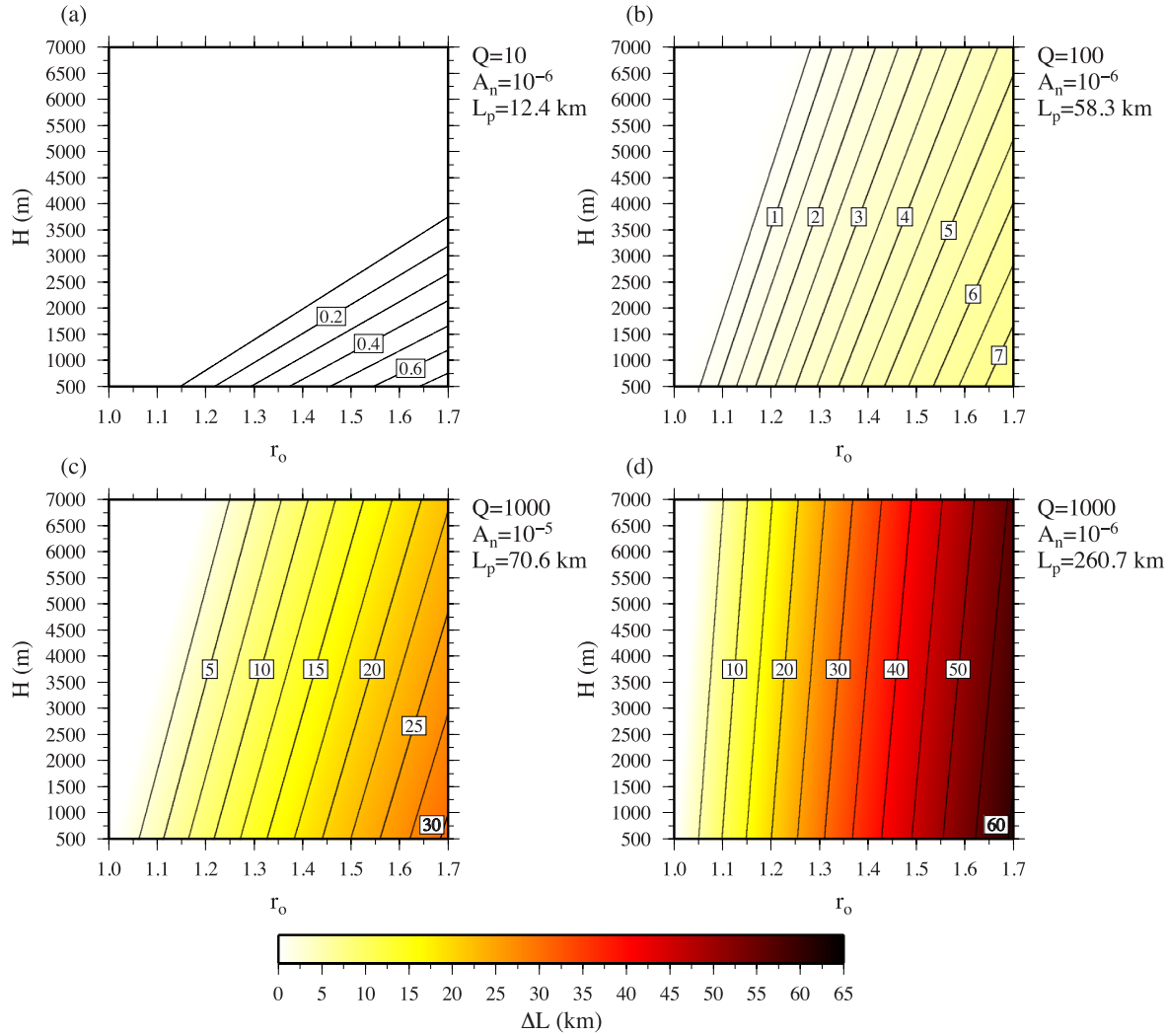


**Figure 5.** Diagrams of $\Delta L$ as a function of $r_0$ and $H$, each for a particular combination of the $Q$ factor and the ambient noise level $A_n$: (a) $Q = 10$, $A_n = 10^{-6}$, (b) $Q = 100$, $A_n = 10^{-6}$, (c) $Q = 1000$, $A_n = 10^{-5}$ and (d) $Q = 1000$, $A_n = 10^{-6}$.

## 4 RESULTS

A total of 445 200 combinations of the four parameters ($F$, $D$, $V_0$ and $G$) were analysed in the first part of the synthetic test yielding the ratios $r_0$. The results were plotted as diagrams of $r_0$ as a function of $F$ and $D$, each for a particular velocity model defined by $V_0$ and $G$. Representative examples are presented in Fig. 4. These diagrams show that $r_0$ decreases with $F$ and its highest values are systematically found for an approximate range between 4 and 10 Hz, a range of frequencies that coincides well with the typical frequency spectrum of most crustal scale WAS experiments, to the point that WAS data are usually filtered for similar frequency bands. Also, $r_0$ decreases for increasing $D$, particularly for high frequencies, and the maximum value is always at $D = 0$ m because $D$ is proportional to the time lapse between the arrivals of the two interfering waves. Because the reflection at the seafloor from water to crust does not involve a phase inversion, the highest two amplitudes interfering at the receiver will occur for the shortest time lapse. Concerning the velocity model, $r_0$ increases with $V_0$, as should be expected on account of the increase in impedance contrast, whereas $G$ has a small influence, and it is not possible to define a clear dependency. For $F = 10$ Hz, the approximate central frequency of the source spectrum in WAS experiments, $r_0$ takes a maximum value of ~1.7 for the $V_0 = 4$ km s$^{-1}$ and $D = 0$ m (Figs 4e and f).

If $r_0$ is smaller than 1, the phenomenon will not occur for that particular parameter combination. However, $r_0$ being greater than 1 does not automatically imply that the phenomenon will occur, because the amplitude-decreasing effects of geometrical spreading and attenuation must be taken into account. To do so, in the second part of the test we sampled $r_0$, $H$ and $L$ to evaluate expressions (8) and (9) for the three different attenuation coefficients ($a_c$) and find their intersections with a series of ambient noise levels ($A_n$) to calculate $\Delta L$. For a given $A_n$–$a_c$ combination, the maximum ray path length for which the primary phase is visible ($L_p$) is constant as eq. (8) does not depend on $r_0$ or $H$. This means that only for ray path lengths greater than $L_p$, the MSRI phase will provide information not available in the primary phase. The diagrams in Fig. 5 show $\Delta L$ as a function of $r_0$ and $H$ for representative $A_n$–$a_c$ combinations. $\Delta L$ increases with $r_0$, as it is proportional to the amplitude of the multiple, and decreases with $H$, because both the effects of attenuation and geometrical spreading grow stronger with this parameter.

For the highest attenuation coefficient ($Q = 10$), and noise levels of $10^{-5}$ or higher, there is no ray path length increment simply because amplitudes remain below the noise level. For the lower noise levels, between $10^{-6}$ and $10^{-9}$, $\Delta L$ stays below 1 km (Fig. 5a).

**Table 3.** The maximum ray path length increments ($\Delta L_{max}$) for every combination of the $Q$ factor and the relative ambient noise level ($A_n$), together with the corresponding maximum ray path length of the primary arrival ($L_p$) and the percentage increment. $L_p$ values marked with an asterisk (∗) are a particular case in which the primary arrival amplitude is below the noise level from the start, that is, from the initial $L_{min} = 10$ km, while the multiple amplitude remains above it for an $L_M = \Delta L + L_{min}$. However, the primary arrival is already below the noise level for $L_p < L_{min}$, which means that $\Delta L$ are in fact bottom limits of the actual achievable increments.

| $Q$ | $A_n$ | $L_p$ (km) | $\Delta L_{max}$ (km) | $\Delta L/L_p$ (per cent) |
|---|---|---|---|---|
| 10 | $10^{-3}$ | – | 0 | 0 |
| 10 | $10^{-4}$ | – | 0 | 0 |
| 10 | $10^{-5}$ | – | 0 | 0 |
| 10 | $10^{-6}$ | 12.4 | 0.76 | 6.1 |
| 10 | $10^{-7}$ | 16.3 | 0.81 | 5.0 |
| 10 | $10^{-8}$ | 20.2 | 0.85 | 4.2 |
| 10 | $10^{-9}$ | 24.3 | 0.87 | 3.6 |
| 100 | $10^{-3}$ | – | 0 | 0 |
| 100 | $10^{-4}$ | 10∗ | 0.87 | 8.7 |
| 100 | $10^{-5}$ | 28.2 | 5.9 | 20.9 |
| 100 | $10^{-6}$ | 58.3 | 7.5 | 12.9 |
| 100 | $10^{-7}$ | 93.3 | 8.3 | 8.9 |
| 100 | $10^{-8}$ | 130.8 | 8.8 | 6.7 |
| 100 | $10^{-9}$ | 169.8 | 9.0 | 5.3 |
| 1000 | $10^{-3}$ | – | 0 | 0 |
| 1000 | $10^{-4}$ | 10∗ | 5.0 | 50 |
| 1000 | $10^{-5}$ | 70.6 | 30.6 | 43.3 |
| 1000 | $10^{-6}$ | 260.7 | 60.7 | 23.3 |
| 1000 | $10^{-7}$ | – | 0 | 0 |
| 1000 | $10^{-8}$ | – | 0 | 0 |
| 1000 | $10^{-9}$ | – | 0 | 0 |

For the intermediate attenuation case ($Q = 100$), there is a gain in ray path length for noise levels of $10^{-4}$ or lower, although $\Delta L$ is still small, always below 10 km (Fig. 5b). As should be expected, the lowest attenuation coefficient ($Q = 1000$) entails the most relevant ray path length increment (Figs 5c and d). However, in terms of noise level it is the most restrictive case: only for $A_n$ between $10^{-4}$ and $10^{-6}$ does it produce an increment in ray path length, whereas above and below this range, both amplitudes are too low and too high, respectively, and never cross the noise level for the 400 km considered. The maximum $\Delta L$ ($\Delta L_{max}$) for $A_n = 10^{-5}$ and $A_n = 10^{-6}$ are 30.6 and 60.7 km, respectively (Table 3). Even though the latter case yields the overall highest $\Delta L_{max}$, judging from their $L_p$ values, 70.6 and 260.7 km, the former can be considered the most profitable of the studied cases. These results are consistent with experimental evidence as for such $L_p$ values most of the ray path is found in the upper mantle were the highest $Q$ values occur.

## 5 DISCUSSION

The synthetic test for our modelling scheme proves that the interference hypothesis is plausible. We have shown that under the appropriate physical conditions, the constructive interference of the multiple with its reflection at the seafloor (MSRI) can produce an arrival with peak amplitude greater than that of the primary wave. The MSRI phase is in fact what we commonly refer to as the multiple on record sections. This mechanism explains the apparent physical paradox occurring in some record sections where multiple phases extend to longer offsets than their primary phases (Fig. 1).

The first part of the test (Fig. 4) shows that the interference systematically attains its highest $r_0$ values within a range of dominant frequency $F$ between 4 and 10 Hz, which coincides with the typical frequency spectrum of marine WAS experiments. Logically, $r_0$ grows for decreasing $D$ distances (in particular for high $F$ values) because this parameter determines the time lapse between the arrivals of the interfering waves at the receiver. Concerning the velocity model, $r_0$ increases with the impedance contrast represented by $V_0$, as more energy is reflected back into the water layer at the seafloor interface.

In the second part of the test, we calculated $\Delta L$ (Fig. 5) as a proxy for the potential offset increment obtained by incorporating the MSRI phase. As could be expected, $\Delta L$ increases with $r_0$ (higher MSRI peak amplitude), decreases with $H$ and $a_c$ (greater amplitude decay) and with $A_n$ (lower SNR). The results show that the phenomenon is only notable in media with a globally low attenuation ($Q$ factor around 1000), and within a SNR range from 100 ($A_n = 10^{-5}$) to 120 dB ($A_n = 10^{-6}$), which explains its relative rareness. For these relevant cases $\Delta L$ reaches maximum values of ∼30 and ∼60 km (Figs 5c and d and Table 3). The relation between ray path length and source–receiver offset is strongly dependent on the subsurface velocity distribution. Still, under usual circumstances, it is reasonable to assume an extension in the offset of the same order of magnitude of $\Delta L$. This offset gain of a few tens of kilometres agrees well with experimental evidence (Fig. 1).

The most adequate geological conditions occur in basement outcrops, for instance, in unsedimented young oceanic crust near mid-ocean ridges (Fig. 1a) or exhumed mantle in extensional basins (Fig. 1b). These geological contexts maximize the seismic impedance contrast at the seafloor, while significantly reducing the general wave attenuation thanks to the absence of water-saturated sediments. Nonetheless, a bathymetry with the appropriate roughness to cause wave scattering in the ∼5–15 Hz frequency range can diminish the effect of the seismic impedance contrast. Therefore, consolidated sedimentary sequences producing a smooth bathymetry may be a propitious setting to observe this phenomenon, as in the Tyrrhenian Basin (Fig. 1b).

Whenever the MSRI phases are longer than the corresponding primary ones, the inclusion of MSRI picks in traveltime modelling increases ray coverage, which results in tomographic models with better resolution. Also, the rays associated to these additional data will potentially have travelled deeper in the subsurface, thus extending the coverage to deeper layers. Since for oceanic crust studies, the average quality WAS data include primary phases associated to rays travelling through the mantle, the possible supplementary MSRI picks would correspond to rays reaching further down into the mantle (see Table 3 for $Q = 1000$). However, given the low-velocity gradient in the mantle, this increase in penetration may be limited. Apart from the extra information, modelling the MSRI phase is useful because it allows to confidently differentiate them from other late arrivals.

## 6 CONCLUSIONS

Based on our synthetic modelling of the MSRI and the calculation of ray path length increments $\Delta L$ as a proxy for the offset gained through the use of MSRI phase, we have drawn the following conclusions:

(1) The MSRI hypothesis explains the *a priori* paradoxical phenomenon of water layer multiple phases extending to longer offsets than their corresponding primary phases (Figs 1 and 2).

(2) The highest amplitude values of the MSRI ($r_0$) are obtained for frequencies $F$ between 4 and 10 Hz, coinciding with the usual frequency spectrum of marine WAS experiments. $r_0$ grows for decreasing receiver–seafloor distances $D$, especially for high $F$, and with the impedance contrast represented by $V_0$ (Fig. 4).

(3) The additional ray path length $\Delta L$, and thus the additional offset to which the MRSI phase is visible with respect to the primary phase in record sections increases with $r_0$, and decreases with $H$, $a_c$ and $A_n$. Relevant values of $\Delta L$ are of some tens of kilometres, in good agreement with experimental evidence (Fig. 1), and are found for low attenuation media ($Q \sim 1000$) and SNRs between 100 and 120 dB (Fig. 5).

(4) The most favourable geological contexts for the phenomenon are given by basement outcrops or consolidated sediments, which enhance the impedance contrast at the seafloor and reduce attenuation because of the lack of a disaggregated, water-saturated sedimentary cover. Also, a subdued bathymetric relief decreases wave scattering, facilitating the occurrence of the phenomenon.

(5) Including the MSRI picks in tomography schemes would improve ray coverage, and consequently, model resolution. Moreover, the corresponding rays will potentially penetrate deeper into the subsurface, increasing the total model depth. Typical marine WAS recordings show primary phases associated to the shallow upper mantle, so that any extra MSRI picks would correspond to deeper mantle layers. Even so, this additional penetration might be limited due to the low-velocity gradient in the mantle. Also, being able to model the MSRI phases can be useful to verify the interpretation of certain phases as late arrivals.

## ACKNOWLEDGEMENTS

This work was conducted under the umbrella of the CSIC-Repsol collaboration project CO-DOS and of the MICINN project POSEIDON (CTM2010–21569) at the Grup de Recerca de la Generalitat de Catalunya, Barcelona Center for Subsurface Imaging (Barcelona-CSI) of the Institut de Ciències del Mar (CSIC). We thank all our colleagues at the Barcelona-CSI for their contributions to the work presented in this manuscript.

## REFERENCES

Backus, M.M., 1959. Water reverberations—their nature and elimination, *Geophysics,* **24**(2), 233–261.

Bharadwaj, P., Wang, X., Schuster, G. & McIntosh, K., 2013. Increasing the number and signal-to-noise ratio of OBS traces with supervirtual refraction interferometry and free-surface multiples, *Geophys J. Int.,* **192,** 1070–1084.

Čevern‌ý, V., 2001. *Seismic Ray Theory,* 1st edn, Cambridge University Press.

Coates, R., 2002. *The Advanced SONAR Course,* Seiche, ISBN:1–904055–01-X.

Courant, R., Friedrichs, K. & Lewy, H., 1967. On the partial difference equations of mathematical physics, *IBM J. Res. Dev.,* **11,** 215–234.

Cummings, J., 2004. *Seismic surveys: what we don't know may hurt*. Report of the Acoustic Ecology Institute prepared for Greenpeace USA.

Dannowski, A., Grevemeyer, I., Phipps Morgan, J., Ranero, C.R., Maia, M. & Klein, G., 2011. Crustal structure of the propagating TAMMAR ridge segment on the Mid-Atlantic Ridge, 21.5°N, *Geochem. Geophys. Geosyst.,* **12,** Q07012, doi:10.1029/2011GC003534.

Dash, R., Spence, G., Hyndman, R.D., Grion, S., Wang, Y. & Ronen, S., 2009. Wide-area imaging from OBS multiples, *Geophysics,* **74**(6), Q41–Q47.

Goldberg, D. & Sun, Y.-F., 1997. Seismic structure of the upper oceanic crust revealed by in situ Q logs, *Geophys. Res. Lett.,* **24,** 333–336.

Goold, J.C. & Fish, P.J., 1998. Broadband spectra of seismic survey air-gun emissions, with reference to dolphin auditory thresholds, *J. acoust. Soc. Am.,* **103,** 2177–2184.

Grad, M., Mjelde, R., Czuba, W., Guterch, A. & Schweitzer, J., 2011. Modelling of seafloor-multiples observed in OBS data from the North Atlantic—new seismic tool for oceanography? *Pol. Polar Res.,* **32**(4), 375–392.

Johnston, D.H. & Toksoz, M.N., 1981. Definitions and terminology, in *Seismic Wave Attenuation,* pp. 1–5, eds Johnston, D.H. & Toksoz, M.N., SEG Geophys, Reprint Ser. No. 2.

Kormann, J., Cobo, P., Recuero, M., Biescas, B. & Sallarès, V., 2009. Modelling seismic oceanography experiments by using first- and second-order complex frequency shifted perfectly matched layers, *Acta Acust. United Ac.,* **95,** 1104–1111.

Kormann, J., Biescas, B., Korta, N., de la Puente, J. & Sallarès, V., 2011. Application of acoustic full waveform inversion to retrieve high-resolution temperature and salinity profiles from synthetic seismic data, *J. geophys. Res.,* **116,** C11039, doi:10.1029/2011JC007216.

Landrø, M. & Amundsen, L., 2010. Marine Seismic Sources Part I, *GeoExpro,* 1, Vol. **7**.

Liu, J.-Y. & Huang, C.-F., 2001. Acoustic plane-wave reflection from rough surface over a random fluid half-space, *Ocean Eng.,* **28,** 751–762.

MacGillivray, A.O. & Chapman, N.R., 2005. *Results from an Acoustic Modelling Study of Seismic Airgun Survey Noise in Queen Charlotte Basin,* School of Earth and Ocean Sciences, University of Victoria.

Minshull, T.A., Muller, M.R. & White, R.S., 2006. Crustal structure of the Southwest Indian Rigde at 66°E: seismic constraints, *Geophys. J. Int.,* **166,** 135–147.

Muller, M.R., Minshull, T.A. & White, R.S., 1999. Segmentation and melt supply at the Southwest Indian Ridge, *Geology,* **27,** 867–870.

Prada, M., Sallarès, V., Ranero, C.R., Guzman, M., Zitellini, N., Grevemeyer, I. & de Franco, R., 2012. Tectonic Structure of the Central Tyrrhenian Sea from wide-angle and near vertical seismics and gravity modelling, in *Proceedings of the AGU Fall Meeting 2012*, T23F-2738, San Francisco, December 3–7, 2012.

Sallarès, V., Charvis, P., Flueh, E.R. & Bialas, J., 2003. Seismic structure of Cocos and Malpelo Volcanic Ridges and implications for hot spot-ridge interaction, *J. geophys. Res.,* **108**(B12), 2564, doi:10.1029/2003JB002431.

Stein, S. & Wysession, M., 2003. *An Introduction to Seismology, Earthquakes, and Earth Structure,* 1st edn, Blackwell Publishing.

Swift, S.A., Lizarralde, D., Stephen, R.A. & Hoskins, H., 1998. Seismic attenuation in upper ocean crust at Hole 504B, *J. geophys. Res.,* **103,** 27 193–27 206.

Urick, R.J., 1983. *Principles of Underwater Sound,* 3rd edn, McGraw-Hill.

White, D.J. & Clowes, R.M., 1994. Seismic attenuation structure beneath the Juan de Fuca Ridge from tomographic inversion of amplitudes, *J. geophys. Res.,* **99,** 3043–3056.

White, R.S., Detrick, R.S., Sinha, M.C. & Cormier, M.H., 1984. Anomalous seismic crustal structure of oceanic fracture zones, *Geophys. J. R. astr. Soc.,* **79,** 779–798.

White, R.S., McKenzie, D. & O'Nions, R.K., 1992. Oceanic crustal thickness from seismic measurements and rare earth element inversions, *J. geophys. Res.,* **97,** 19 683–19 715.

Wilcock, W.S.D., Solomon, S.C., Purdy, G.M. & Toomey, D.R., 1992. The seismic attenuation structure of a fast-spreading mid-ocean ridge, *Science,* **258,** 1470–1474.

Wilcock, W.S.D., Solomon, S.C., Purdy, G.M. & Toomey, D.R., 1995. Seismic attenuation structure of the East Pacific Rise near 9°30'N, *J. geophys. Res.,* **100,** 24 147–24 165.